CR303
May 2, 1997

Recent LEP2 Results from OPAL

D. Glenzinski
Enrico Fermi Institute, University of Chicago
Chicago Illinois, U. S. A. 60637

PACS numbers:01.30.Cc, 12.20.Fv, 14.70.Fm, 14.80.Bn, 14.80.Ly, 14.80-j

In 1996, after another set of upgrades, LEP began running for the first time at center-of-mass energies above the W-pair threshold. This new energy regime offers a wide array of physics topics including tests of the Standard Model at higher energy scales, search physics, and W physics. We summarize the recent results from OPAL using 9.9 pb $^{-1}$ of data collected at $\sqrt{s} = 161.3$ GeV from June to August 1996.

1. Introduction

In October of 1995 the very fruitful LEP1 physics program was officially brought to an end. Later that same year, LEP saw its first running at center-of-mass energies significantly above the Z^0-peak ($\sqrt{s} \geq 130$ GeV). In 1996, after another set of upgrades, LEP began running at center-of-mass energies above the W-pair threshold ($\sqrt{s} > 2M_W$). This new energy regime offers a wide array of physics topics including tests of the Standard Model (SM) at higher energy scales, search physics, and W physics. We summarize the recent results from OPAL using 9.9 pb $^{-1}$ of data collected at $\sqrt{s} = 161.3$ GeV from June to August 1996. The OPAL detector is described in detail in reference [1].

2. QCD Physics at LEP2

The increased center-of-mass energy at LEP offers a new energy scale at which to test the Standard Model, and in particular to test the predicted effects from the running of α_{strong} via QCD observables. At center-of-mass energies significantly above the Z^0-peak, initial state radiation (ISR) effects become large so that the effective center-of-mass of the e^+e^- interaction, $\sqrt{s'}$, is less than the full energy available, $\sqrt{s} = 2E_{\text{beam}}$. In order to test the SM at a new energy scale it is necessary to differentiate full energy events, in which $\sqrt{s'} \approx \sqrt{s}$, from events with a significant amount of initial state radiation - in particular the dominant "radiative return" events in which $\sqrt{s'} \approx M_{Z^0}$. This is accomplished with a kinematic fit that calculates, for each event, an $\sqrt{s'}$ using the visible energy and momentum measured in the event, and assuming energy and momentum conservation as described in reference [2]. The fit uses observed isolated photons and allows up to two unobserved ISR photons whose directions are taken to be along the beam axis. The resulting $\sqrt{s'}$ distribution is shown in Figure 1 for events passing a high multiplicity pre-selection [3]. The so-called "radiative return" events give rise to a peak centered about the Z^0 mass. To select full energy events we require that $\sqrt{s} - \sqrt{s'} < 10$ GeV. This yields 307 events with an estimated 6% background from various 4-fermion processes (mostly W^+W^- events) and approximately a 5% background from mismeasured radiative events [4]. For several QCD event shape variables we compare the data to a variety of Monte Carlo generators, which employ a variety of fragmentation schemes. Figure 2 shows these comparisons for the thrust, thrust major and minor, oblateness, sphericity, and aplanarity event shape variables. Using a combined fit to a set of separate variables whose dependence on α_{strong} is predicted by NLLA QCD [5], we measure $\alpha_{\text{strong}}(161\text{GeV}) = 0.101 \pm 0.005(\text{stat.}) \pm 0.007(\text{syst.})$. This measurement is

compared to the QCD prediction [6] in Figure 3. In addition we measure the mean charged particle multiplicity to be $< n_{ch} > (161 GeV) = 24.46 \pm 0.45(stat.) \pm 0.44(syst.)$ and the position of the peak in the $\xi_p = \ln(1/x_p)$ distribution to be $\xi_0(161 GeV) = 4.00 \pm 0.03(stat.) \pm 0.02(syst.)$. These measurements are compared to data taken at lower center-of-mass energies in Figures 4 and 5. These analyses are fully described in reference [4].

3. Two Fermion Physics at LEP2

Hadronic and leptonic two fermion events can also be used to test the SM at the higher energies available at LEP2. We measure cross-sections and asymmetries both including and excluding the dominant radiative return events, $e^+e^- \rightarrow \gamma Z^0$, using the event selections described in Reference [7]. For the $\mu^+\mu^-$, $\tau^+\tau^-$, and $q\bar{q}$ final states, we estimate the effective center-of-mass energy, $\sqrt{s'}$, in a manner similar to the one described above, in order to discriminate full energy events, $\sqrt{s'} \approx \sqrt{s}$, from the radiative return events, $\sqrt{s'} \approx M_{Z^0}$. An inclusive sample is defined by the cut $s'/s > 0.01$ and an exclusive sample by the cut $s'/s > 0.80$. In the e^+e^- final state, due to the dominant t-channel production diagram, a definition of $\sqrt{s'}$ as in the other final states is not meaningful. Events with little radiation are therefore selected by a cut on the acollinearity angle between the electron and positron, $\theta_{acol} = \pi - \theta_{e^+e^-}$. A cut of $\theta_{acol} < 10°$ roughly corresponds to a cut of $s'/s > 0.80$ for the s-channel contribution. A sample with a smaller t-channel contribution is identified by requiring the observed electron to satisfy the condition $|\cos\theta_{e^-}| < 0.70$. The observed number of events, measured cross-sections, and corresponding SM predictions are shown in Table 1. These same results are shown in comparison with lower energy data in Figure 6. For the lepton-pair events we also measure the forward-backward asymmetry. The results are shown graphically in Figure 7, along with the lepton angular distributions, and agree with the SM predictions. For the non-radiative hadronic events we also measure R_b, the fraction of hadronic events which decay into a $b\bar{b}$ pair, using a secondary-vertex tagging method similar to the one described in Reference [8]. We find $R_b(161 GeV) = 0.141 \pm 0.028(stat.) \pm 0.012(syst.)$. Figure 8 plots R_b as a function of center-of-mass energy for the three OPAL measurements at LEP1 [8], LEP1.5, and this measurement. All three measurements are within one standard deviation of the SM expectation.

These analyses are described in detail in Reference [7].

4. Search Physics at LEP2

2 fermions	Sel. events	σ (pb)	σ^{SM} (pb)
Hadrons ($s'/s > 0.01$)	1472	$152 \pm 4 \pm 2$	149
Hadrons ($s'/s > 0.8$)	370	$35.3 \pm 2.0 \pm 0.7$	33.2
e^+e^- ($|\cos\theta_{e^-}| < 0.70$, $\theta_{\mathrm{acol}} < 10°$)	285	$28.1 \pm 1.7 \pm 0.2$	28.1
e^+e^- ($|\cos\theta_{e^\pm}| < 0.96$, $\theta_{\mathrm{acol}} < 10°$)	4447	$435 \pm 7 \pm 6$	424
e^+e^- ($|\cos\theta_{e^\pm}| < 0.90$, $\theta_{\mathrm{acol}} < 170°$)	1582	$158 \pm 4 \pm 2$	153
$\mu^+\mu^-$ ($s'/s > 0.01$)	98	$12.5 \pm 1.2 \pm 0.5$	11.3
$\mu^+\mu^-$ ($s'/s > 0.8$)	44	$4.6 \pm 0.7 \pm 0.2$	4.5
$\tau^+\tau^-$ ($s'/s > 0.01$)	64	$15.7 \pm 2.0 \pm 0.7$	11.3
$\tau^+\tau^-$ ($s'/s > 0.8$)	43	$6.7 \pm 1.0 \pm 0.3$	4.5

Table 1. Numbers of events and measured cross-sections at $\sqrt{s} = 161.3$ GeV. For the cross-sections, the first error is statistical and the second is systematic. The last column shows the SM cross-section predictions from ZFITTER [9] ($q\bar{q}$, $\mu^+\mu^-$, and $\tau^+\tau^-$) and ALIBABA [10] (e^+e^-).

The increased center-of-mass energy at LEP2 opens up an entirely new region of parameter space for a variety of possible new physics signatures. OPAL has a wide and varied program in order to be as sensitive to as many topologies as possible. The principal signature is that of missing momentum ($\not{P}$) plus a pair of acoplanar jets, leptons, or some combination thereof. These simple topologies allow sensitivity to SM Higgs, Supersymmetric (SUSY) Higgs, chargino, neutralino, slepton, stop, sbottom, excited lepton, and both charged and neutral heavy lepton production processes. By including 4-jet topologies, and exploiting for particular search channels the presence of hard photons, b-jets, and/or resonances, OPAL achieves reasonable efficiencies over a large parameter space for many models. No significant excess is observed in any of our searches, and a variety of limits are set at the 95% confidence level. Although there are OPAL results for all of the above mentioned processes [11], I will only discuss here the results obtained from the SM Higgs, the chargino and neutralino, and the anomalous 4-jet production searches.

4.1. **Search for the Standard Model Higgs Boson**

The higher center-of-mass energy available at LEP2 increases the sensitivity of the search for a SM Higgs boson. At this centre-of-mass energy, the main production process for the SM Higgs boson is $e^+e^- \to Z^0H^0$. The dominant decay is $H^0 \to b\bar{b}$, with a branching ratio of approximately 86%. Other relevant decay modes are: $H^0 \to \tau^+\tau^-$ (8%), $H^0 \to c\bar{c}$ (4%), and

H^0	Z^0	Eff (%)	N_{bkg}	N_{obs}
$b\bar{b}$	$q\bar{q}$	23	0.8	1
$q\bar{q}$	$\nu\bar{\nu}$	46	0.9	1
$q\bar{q}$	$\tau^+\tau^-$	20	0.2	0
$q\bar{q}$	$\ell\bar{\ell}$	65	0.1	0

Table 2. The channel by channel efficiency for a Higgs boson of mass $M_H = 65$ GeV is given along with the number of expected background events from SM processes. The number of observed events is also given and is consistent with the background expectation.

$H^0 \rightarrow$ gluons (2%) [12]. In the mass range of interest, these branching ratios exhibit only a mild dependence on the Higgs boson mass.

The OPAL search is sensitive to the principal final state topologies, namely: (i) the four-jet channel, $e^+e^- \rightarrow Z^0H^0 \rightarrow q\bar{q}b\bar{b}$; (ii) the missing energy channel, mainly from $e^+e^- \rightarrow Z^0H^0 \rightarrow \nu\bar{\nu}q\bar{q}$, but including a small contribution from the W^+W^- fusion process $e^+e^- \rightarrow \nu\bar{\nu}H^0$; (iii) the tau channels, $e^+e^- \rightarrow Z^0H^0 \rightarrow \tau^+\tau^-q\bar{q}$ and $q\bar{q}\tau^+\tau^-$; and (iv) the electron and muon channels, predominantly from $e^+e^- \rightarrow Z^0H^0 \rightarrow e^+e^-q\bar{q}$ and $\mu^+\mu^-q\bar{q}$, but including a small contribution from the Z^0Z^0 fusion process $e^+e^- \rightarrow e^+e^-H^0$. These topologies account for about 95% of all Higgs boson final states.

Table 2 lists the typical efficiency for each channel and gives the observed and expected number of background events for the approximately 10 pb^{-1} of data collected at $\sqrt{s} = 161$ GeV. The observations are in good agreement with the number of expected events from Standard Model background processes. By combining this data with data taken at $\sqrt{s} \approx M_{Z^0}$, we derive a lower limit on the mass of the Higgs boson of $M_{H^0} > 65.0$ GeV at the 95% confidence level. This limit is shown in Figure 9.

A more detailed description of this analysis can be found in Reference [13].

4.2. Search for Chargino and Neutralino Production

We perform a direct search for the pair production of charginos and neutralinos, whose existence is predicted in SUSY theories. Charginos, $\tilde{\chi}_j^{\pm}$, are the mass eigenstates formed by the mixing of the fields of the fermionic partners of the charged gauge bosons (winos) and those of the charged Higgs bosons (charged higgsinos). Fermionic partners of the photon, the Z boson, and the neutral Higgs bosons mix to form the mass eigenstates called neutralinos, $\tilde{\chi}_i^0$. In each case, the index j or i increases with increasing mass.

		$\not{P}$ + Acoplanar :		
		jets	jets $+\,\ell$	leptons
$\tilde{\chi}_1^{\pm}$	small$\Delta\mathrm{M}_{\pm}$	$10-20\%$	$15-20\%$	$11-24\%$
	large $\Delta\mathrm{M}_{\pm}$	$40-60\%$	$30-65\%$	—
	BR	45%	45%	10%
$\tilde{\chi}^0$	small$\Delta\mathrm{M}_0$	$5-20\%$	—	$5-22\%$
	large $\Delta\mathrm{M}_0$	$20-45\%$	—	—
	BR	$40-80\%$		$20-60\%$
0.7 ± 0.2 expected background				
2 events observed				

Table 3. Typical efficiencies for the various topologies used in the chargino and neutralino searches along with the number of expected events from SM processes. The number of observed events is consistent with this background expectation.

If charginos are light enough, they can be pair produced in e^+e^- collisions through γ or Z^* exchange in the s-channel and sneutrino ($\tilde{\nu}$) exchange in the t-channel. Neutralino pairs ($\tilde{\chi}_i^0\tilde{\chi}_j^0$) can be produced through an s-channel γ or Z^* exchange, or by t-channel selectron ($\tilde{e}$) exchange.

We assume that the lightest neutralino, $\tilde{\chi}_1^0$, is the lighest supersymmetric particle and that R-parity is conserved. Experimentally these assumptions have the consequence that the $\tilde{\chi}_1^0$ is stable and invisible. The lightest chargino, $\tilde{\chi}_1^{\pm}$, can then decay via $\tilde{\chi}_1^{\pm} \rightarrow \tilde{\chi}_1^0\ell^+\nu$ or $\tilde{\chi}_1^{\pm} \rightarrow \tilde{\chi}_1^0 q\overline{q}'$ while the $\tilde{\chi}_2^0$ can then decay into the final states $\tilde{\chi}_1^0\nu\overline{\nu}$, $\tilde{\chi}_1^0\ell^+\ell^-$, or $\tilde{\chi}_1^0 q\overline{q}$. These assumptions have the additional consequence that since events of the type $e^+e^- \rightarrow \tilde{\chi}_1^0\tilde{\chi}_1^0\gamma$ would suffer from a large irreducible background from the standard model process $e^+e^- \rightarrow \nu\overline{\nu}\gamma$, we can only achieve a reasonable sensitivity for events of the type $e^+e^- \rightarrow \tilde{\chi}_2^0\tilde{\chi}_1^0$, and $e^+e^- \rightarrow \tilde{\chi}_3^0\tilde{\chi}_1^0$. Note that the final state kinematics, and therefore the detection efficiencies, will depend on the mass difference between the chargino and the lightest neutralino, $\Delta\mathrm{M}_{\pm} = \mathrm{M}(\tilde{\chi}_1^{\pm}) - \mathrm{M}(\tilde{\chi}_1^0)$. Similarly for the neutralinos, whose detection efficiency will depend upon the mass difference $\Delta\mathrm{M}_0 = \mathrm{M}(\tilde{\chi}_2^0) - \mathrm{M}(\tilde{\chi}_1^0)$.

Typical efficiencies for the various final state topologies are given in Table 3 along with the total number of observed and expected events. No significant excess is observed. Table 4 gives the 95% confidence level lower limits that we extract in the context of the Minimal Supersymmetric Standard Model (MSSM) theory assuming that $\Delta\mathrm{M}_{\pm} > 10$ GeV and $\Delta\mathrm{M}_0 > 10$ GeV. Figure 10 shows the 95% confidence level upper limit cross-section contours for $\tilde{\chi}_1^+\tilde{\chi}_1^-$ and $\tilde{\chi}_2^0\tilde{\chi}_1^0$ production assuming the decays $\tilde{\chi}_1^{\pm} \rightarrow \tilde{\chi}_1^0 \mathrm{W}^{*\pm}$ and $\tilde{\chi}_2^0 \rightarrow \tilde{\chi}_1^0 \mathrm{Z}^*$ occur with 100% branching fraction.

A more detailed description of this analysis can be found in Refer-

Mass	$\tan\beta = 1.5$		$\tan\beta = 35$	
(GeV)	Min. m_0	m_0=1 TeV	Min. m_0	m_0=1 TeV
$M_{\tilde\chi_1^\pm}$	62.0	78.5	66.5	78.8
$M_{\tilde\chi_1^0}$	12.0	30.3	35.8	41.3
$M_{\tilde\chi_2^0}$	45.3	51.9	67.2	80.0
$M_{\tilde\chi_3^0}$	86.3	94.3	112.5	112.5

Table 4. Lower limits on chargino and neutralino masses at the 95% confidence level in the context of the MSSM and assuming $\Delta M > 10$ GeV. The limits are derived for both the minimal m_0 consistent with present experimental constraints and $m_0 = 1$ TeV for the two cases $\tan\beta = 1.5$ and $\tan\beta = 35$. The limits on the $\tilde\chi_3^0$ mass are obtained mainly from excluded regions in the MSSM parameter space resulting from the direct search for lighter neutralinos and $\tilde\chi_1^\pm$.

ence [14].

4.3. Anomalous Four-Jet Production

Using LEP1.5 data, the ALEPH collaboration reported a large excess of four-jet events [15]. We have performed an analogous analysis sensitive to anomalous four-jet production. Using a sample of simulated SUSY $h^0A^0 \to qqqq$ ($\sqrt{s} = 133$ GeV) as a benchmark for comparison, we achieve the same efficiency and background and a comparable mass resolution (to within 10%) as the ALEPH analysis, thus ensuring that the two analyses have the same sensitivity. For each event passing the cuts, the invariant mass of each jet-jet pair is calculated for all possible jet-jet combinations. The sum of the di-jet masses for that combination yielding the minimum mass difference between the two pairings is shown in Figure 11, which includes all data taken at the center-of-mass energies 133, 161, and 172 GeV. We expect 26.0 events and observe 20. The distribution of the sum of the di-jet masses is consistent with the SM background expectation. If systematic effects are neglected, the ALEPH and OPAL data are consistent at the level of $\sim 10^{-6}$. It should be noted that the inclusion of the systematic effects would reduce this significance.

5. WW Physics at LEP2

At the center-of-mass energy $\sqrt{s} = 161$ GeV the W^+W^- production cross-section is dominated by the so called "CC03" diagrams [16]: s-channel γ or Z^* exchange, and t-channel neutrino exchange. This center-of-mass

energy lies just above the W pair production threshold, and the cross-section here has a particularly strong dependence on the value of the mass of the W-boson, M_W, so that it is possible to extract M_W from the data by measuring the cross-section and comparing with theoretical predictions in the context of the SM. These measurements are complementary to those at the Tevatron collider [17] and to those which will be performed during the later phases of LEP2 operation by directly reconstructing the W decay products. In addition, the two s-channel contributions to the cross-section are sensitive to the triple gauge couplings, WWZ and $WW\gamma$.

5.1. Measurement of the W Boson Mass

The analysis is sensitive to all expected decay topologies, the fully hadronic decays, $W^+W^- \rightarrow q\overline{q}q\overline{q}$, the semi-leptonic decays, $W^+W^- \rightarrow q\overline{q}\ell\nu$, and the fully leptonic decays, $W^+W^- \rightarrow \ell\nu\ell\nu$ ($\ell = e$, μ, or τ). The dominant background is $Z^0/\gamma \rightarrow f\overline{f}$, where f is any charged fermion. Other backgrounds arise from four-fermion processes which do not contain two resonant W bosons in the intermediate state. These four-fermion backgrounds fall into two classes: those which can interfere with the W^+W^- four-fermion states, and those which cannot. The interfering four-fermion backgrounds are particularly problematic because they can also depend on M_W. This mass-dependent four-fermion background is taken into account when extracting M_W from the observed data. In addition, the cross-section for the process $e^+e^- \rightarrow W^+W^-$, arising from the CC03 diagrams, is also measured from the data assuming that the interference terms have only a small effect on the accepted W^+W^- cross-section. This is a reasonable assumption given the current level of statistical precision.

Fully hadronic $W^+W^- \rightarrow q\overline{q}q\overline{q}$ events are selected as high-multiplicity, spherical, four-jet events, whose kinematics are compatible with the $e^+e^- \rightarrow W^+W^-$ hypothesis. The semi-leptonic $W^+W^- \rightarrow q\overline{q}\ell\nu$ events are characterized by two, high-multiplicity, back-to-back jets, an energetic lepton candidate (a low multiplicity jet in the case of $\ell = \tau$), and large missing transverse momentum due to the escaping neutrino. The fully-leptonic decays, $W^+W^- \rightarrow \ell\nu\ell\nu$ are selected as energetic, acoplanar, lepton pairs with large missing transverse momentum. The efficiencies, and expected number of signal (assuming the world average W-boson mass [18]) and background events for each channel are given in Table 5.1. Summing over all channels, we expect 27.6 ± 2.5 events and observe 28.

By neglecting the M_W dependence of the interfering four-fermion backgrounds, we can measure the W-pair (CC03) production cross-section using the information from each channel separately. For each channel, the probability of obtaining the number of observed events is calculated as a

Channel	Eff (%)	expected			Obs
		Signal	Bkgd	Total	
qqqq	57	9.6	3.4	13.0 ± 1.1	14
qqeν	71	3.9	0.2	4.1 ± 0.5	3
qq$\mu\nu$	77	4.2	0.2	4.5 ± 0.5	2
qq$\tau\nu$	42	2.3	1.0	3.2 ± 0.4	7
$\ell\nu\ell\nu$	65	2.6	0.2	2.8 ± 0.3	2
Total	61	22.6	5.0	27.6 ± 2.5	28

Table 5. The efficiency, background, and number of observed events for each of the WW final state topologies. The efficiency is calculated assuming the world average W mass and taking as signal only the CC03 diagrams. The backgrounds correspond to all other diagrams and assumes that the interference effects can be neglected.

function of the W^+W^- cross-section using Poisson statistics and assuming SM branching ratios. A likelihood is formed from the product of the Poisson probabilities for each channel. The maximum likelihood value yields a CC03 cross-section of

$$\sigma_{WW} = 3.62^{+0.93}_{-0.82}(\text{stat}) \pm 0.16(\text{syst})\text{pb}. \tag{1}$$

The systematic uncertainty is evaluated by means of repeated MC trials. The procedure takes into account the correlated luminosity uncertainties and the small correlated systematic uncertainties between the semi-leptonic channels.

To determine the W-boson mass we parameterize the total accepted cross-section for each channel, including the effects of interfering four-fermion final states, as a function of M_W as shown in Figure 12. We employ a maximum likelihood technique analogous to the one described above to determine

$$M_W = 80.80^{+0.44+0.09}_{-0.41-0.10} \pm 0.03\text{GeV}, \tag{2}$$

where the first and second uncertainties are statistical and systematic, respectively, and the third arises from the current estimate of the LEP beam energy uncertainty. As a cross-check, the value of M_W can also be determined from the CC03 cross-section measurement described above by employing the semi-analytic program GENTLE [19] to derive the dependence

of σ_{WW} on M_W, and by assuming that the experimental acceptance does not significantly vary as a function of M_W. The W^+W^- cross-section and resulting M_W measured in this CC03 framework are shown in Figure 13. This measurement is consistent with the value determined in the full four-fermion analysis.

This analysis is described in more detail in Reference [20].

5.2. Measurement of the Triple Gauge Couplings

Anomalous triple gauge couplings (TGCs) can affect both the total production cross-section and the shape of the differential cross-section as a function of the W production angle. The relative contributions of each helicity state of the W-bosons are also changed, which in turn affects the distributions of their decay products.

The most general Lorentz invariant Lagrangian has up to 14 independent WWV couplings. Requiring electromagnetic gauge invariance and C and P invariance reduces this parameter set to five, 3 describing the WWZ vertex and 2 desciding the WWγ vertex. This parameter space can be further reduced by considering constraints available from lower energy data and precise measurements at LEP1 [16]. As a result of these considerations, three specific linear combinations of these couplings have been proposed which are not tightly constrained by the lower energy data. These are:

$$\alpha_{B\phi} \equiv \Delta\kappa_\gamma - \Delta g_1^z \cos^2\theta_w$$
$$\alpha_{W\phi} \equiv \Delta g_1^z \cos^2\theta_w$$
$$\alpha_W \equiv \lambda_\gamma$$

with the constraints that $\Delta\kappa_z = \Delta g_1^z - \Delta\kappa_\gamma tan^2\theta_w$ where the Δ indicates the deviation of the respective quantity from the SM expectation and θ_w is the weak mixing angle. We are most sensitive to the Wϕ model, which is the only model we presently consider assuming $\alpha_{B\phi}$ and α_W are zero.

We use both the total cross-section and relevant differential kinematic distributions to set limits on $\alpha_{W\phi}$. For the cross-section analysis, the same selections are used as described in Section 5.1. For the analysis of the kinematic distributions we use only the q$\bar{q}\ell\nu$ channels since - in contrast with the q$\bar{q}$q$\bar{q}$ channel - there is neither an ambiguity in assigning decay fermion pairs to each W, nor in determining the charges of each W. These selections are augmented in order to further reduce the background. The kinematic variables used are:

1. $\cos\theta_W$, the production angle of the W^- with respect to the e^- beam direction,

2. p_W, the momentum of the hadronically decaying W

3. $\cos\theta_\ell^*$, the polar decay angle of the charged lepton with respect to the W flight direction measured in the W rest frame

4. ϕ_ℓ^*, the azimuthal decay angle of the charged lepton with respect to a plane defined by the W and the beam axis.

In the case of the $q\bar{q}e\nu$ and $q\bar{q}\mu\nu$ channels we use variables resulting from a kinematic fit demanding energy and momentum conservation. For the $q\bar{q}\tau\nu$ channel we use energy and momentum constraints to calculate the energy of the of the τ where the τ flight direction is approximated by the direction of its observed decay products. As demonstrated in Figure 14, the resolution of the kinematic variables, as estimated from MC, is comparable for all the $q\bar{q}\ell\nu$ channels.

The total cross-section measurement is used to calculate a likelihood, analogous to the one described in Section 5.1, except that σ_{WW} is parameterized as a function of $\alpha_{W\phi}$, assuming the world average M_W. For the differential distributions, we calculate the likelihood for the observed $q\bar{q}\ell\nu$ events to have their measured distributions of the kinematic variables as a function of $\alpha_{W\phi}$. These likelihoods are independent and are added together to yield a total likelihood distribution, shown in Figure 15, from which we measure

$$\alpha_{W\phi} = -0.61^{+0.73}_{-0.61}(\text{stat}) \pm 0.35(\text{syst}). \tag{3}$$

The corresponding 95% confidence level limits are

$$-2.1 < \alpha_{W\phi} < 1.6 \tag{4}$$

This analysis is described in more detail in Reference [21].

6. Summary

During the 1996 data taking run LEP ran for the first time at center-of-mass energies above the W-pair production threshold. This new energy regime offers new tests of the SM, opens up a previously unexplored region of parameter space for a wide variety of models beyond the SM, such as SUSY, and affords the first study of W^+W^- events from which we can measure M_W and extract limits for anomalous triple gauge couplings. OPAL has established a wide and varied physics program exploiting these opportunities [4] [7] [11] [13] [14] [20] [21].

REFERENCES

[1] OPAL Collab. K. Ahmet et al. Nucl. Instrum. Methods **A305** (1991) 251.

[2] OPAL Collab. G. Alexander et al. Z. Phys. **C72** (1996) 191.

[3] OPAL Collab. G. Alexander et al. Z. Phys. **C52** (1991) 175.

[4] OPAL Collab. K. Ackerstaff et al. CERN-PPE/97-015 Submitted to, Z. Phys.

[5] S. Cantani, L. Trentadue, G. Turnock, and B. R. Webber, Nucl. Phys. **B407** (1993) 3; S. Cantani, G. Turnock, B. R. Webber, Phys. Lett. **B295** (1992) 269; G. Dissertori and M. Schmelling, Phys. Lett. **B361** (1995) 167.

[6] C. T. H. Davies et al. Phys. Lett. **B345** (1995) 42; G. P. Lepage, hep-lat/9607076 (1996).

[7] OPAL Collab. K. Ackerstaff et al. Phys. Lett. **B391** (1997) 221.

[8] OPAL Collab. K. Ackerstaff et al. CERN-PPE/96-137 to be published in Z. Phys.

[9] D. Bardin et al. CERN-TH 6443/92 (May 1992); Phys. Lett. **B255** (1991) 290; Nucl. Phys. **B351** (1991) 1; Z. Phys. **C44** (1989) 493.

[10] W. Beenakker et al. Nucl. Phys. **B349** (1991) 323.

[11] OPAL Collab. K. Ackerstaff et al. CERN-PPE/96-182, to be published in Phys. Lett. B; Phys. Lett. **B393** (1997) 217; Phys. Lett. **B391** (1997) 197; Phys. Lett. **B391** (1997) 210; Phys. Lett. **B389** (1996) 197.

[12] A. Djouadi, M. Spira, and P. M. Zerwas, Z. Phys. **C70** (1996) 425.

[13] OPAL Collab. K. Ackerstaff et al. Phys. Lett. **B393** (1997) 231.

[14] OPAL Collab. K. Ackerstaff et al. Phys. Lett. **B389** (1996) 616.

[15] ALEPH Collab. D. Buskulic et al. Z. Phys. **C71** (1996) 179.

[16] Proceedings of CERN LEP2 Workshop, CERN 96-01, W. Beenakker et al. eds. G. Altarelli, F. Zwirner, February 1996.

[17] D0 Collaboration, S. Abachi et al. Phys. Rev. Lett. **77** (1996) 3309; CDF Collaboration, F. Abe et al. Phys. Rev. Lett. **75** (1995) 11, Phys. Rev. **D52** (1995) 4784.

[18] The Particle Data Group, R. M. Barnett et al. Phys. Rev. **D54** (1996) 1.

[19] D. Bardin et al. Nucl. Phys. B, Proc. Suppl. **37B** (1994) 148.

[20] OPAL Collab. K. Ackerstaff et al. Phys. Lett. **B389** (1996) 416.

[21] OPAL Collab. K. Ackerstaff et al. CERN-PPE/97-04, to be published in Phys. Lett. B.

[22] S. Bethke, PITHA 96/30 (1996), Talk presented at the QCD Euroconference, Montpellier, France July 4-12 1996.

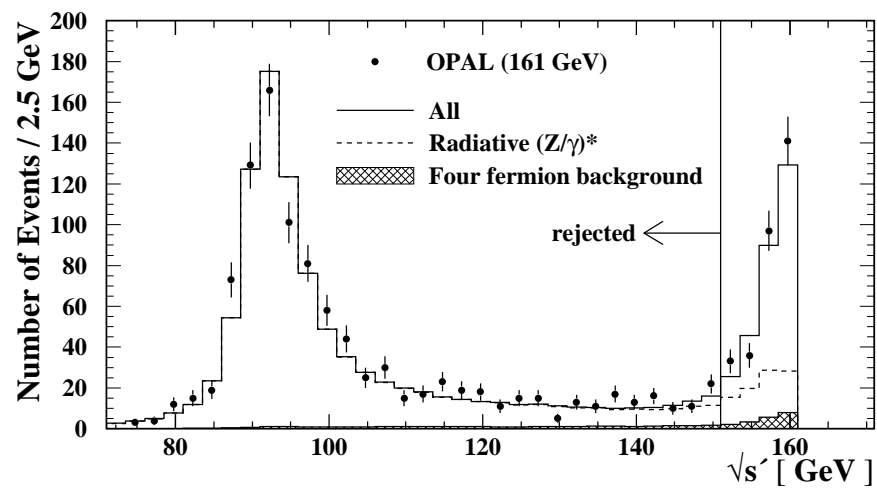[23] OPAL Collab. G. Alexander et al. Phys. Lett. **B377** (1996) 181.

Fig. 1. Distribution of $\sqrt{s'}$ for the data (full points) with statistical errors. The Monte Carlo predictions for the $e^+e^- \rightarrow Z/\gamma$ events (solid line), the radiative background (dashed line), and the 4-fermion background (hatched) are also shown.
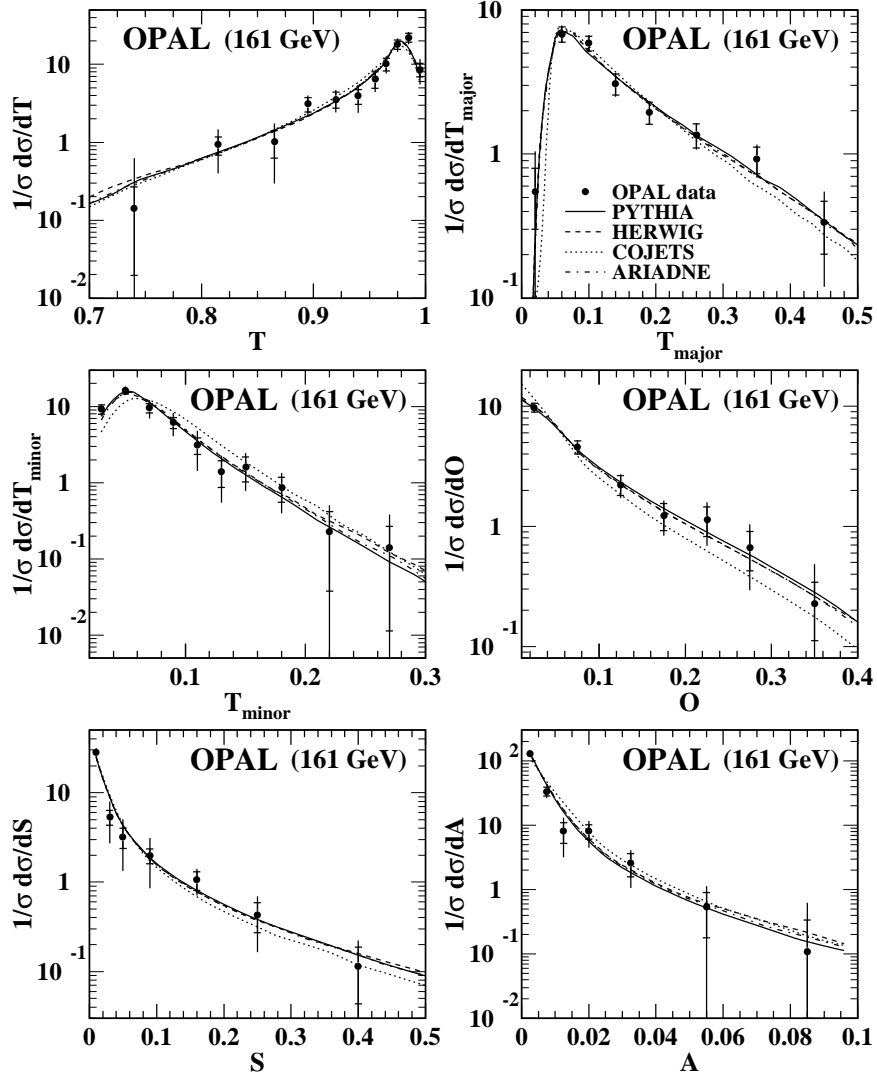
Fig. 2. Distributions of the event shape variables thrust (T), thrust major, (T_{major}), thrust minor (T_{minor}), oblateness (O), sphericity (S), and aplanarity (A). Experimental statisitical error bars are delimited by the small horizontal bars. The total errors are shown by the vertical error lines. Predictions from several Monte Carlo generators are also shown.

14
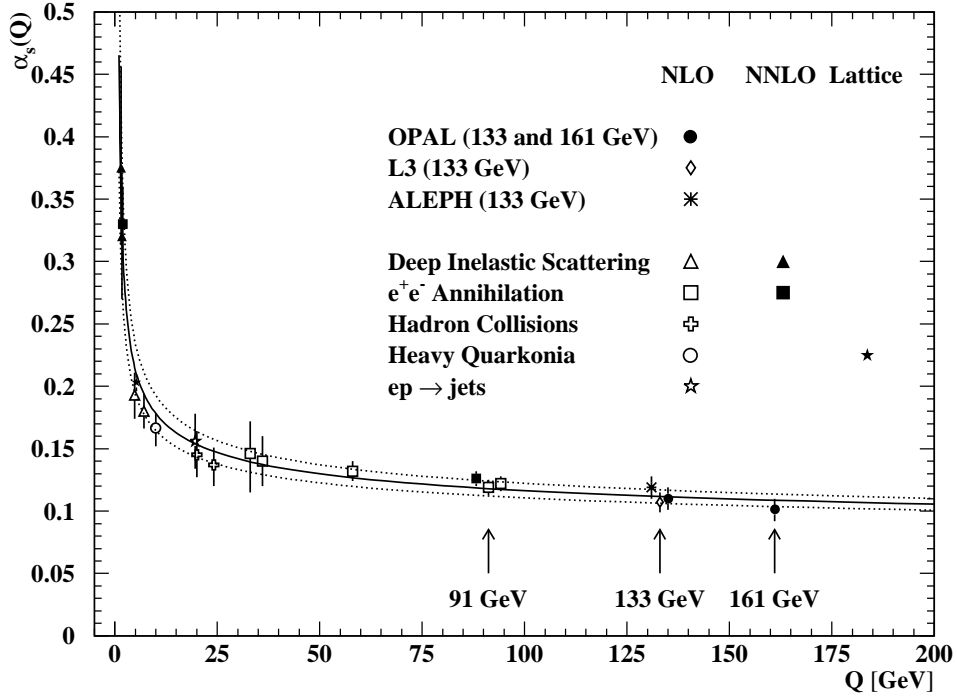
Fig. 3. Values of α_{strong} as a function of energy [22]. The labels NLO and NNLO refer to the order of calculation used. NLO corresponds to $\mathcal{O}(\alpha_{\mathrm{strong}}^2)$ in e^+e^- annihilations, and NNLO to $\mathcal{O}(\alpha_{\mathrm{strong}}^3)$. The label Lattice refers to α_{strong} values determined from lattice QCD calculations. The curve shows the $\mathcal{O}(\alpha_{\mathrm{strong}}^3)$ QCD prediction for $\alpha_{\mathrm{strong}}(\mathcal{Q})$ using $\alpha_{\mathrm{strong}}(M_Z) = 0.118 \pm 0.006$; the full line shows the central value while the dotted lines indicate the variation given by the uncertainty.
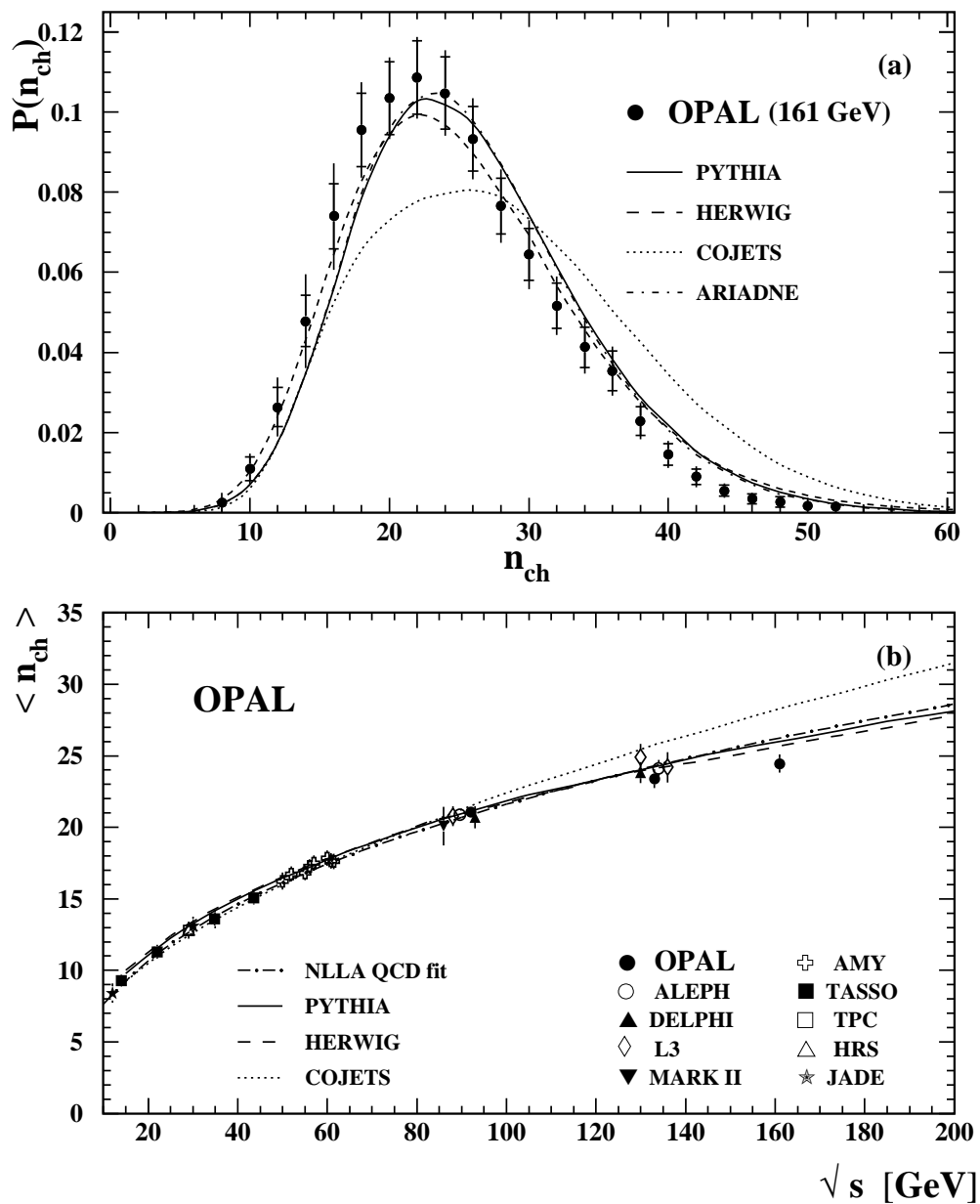
Fig. 4. (a) Corrected distribution of the charged particle multiplicity n_{ch}. Predictions from several Monte Carlo generators are also shown. (b) Mean charged particle multiplicity measurements as a function of $\sqrt{s}$. The measurements are compared to a fit of the NLLA QCD prediction for the evolution of the charged particle multiplicity with $\sqrt{s}$ and to the predictions of several Monte Carlo generators.
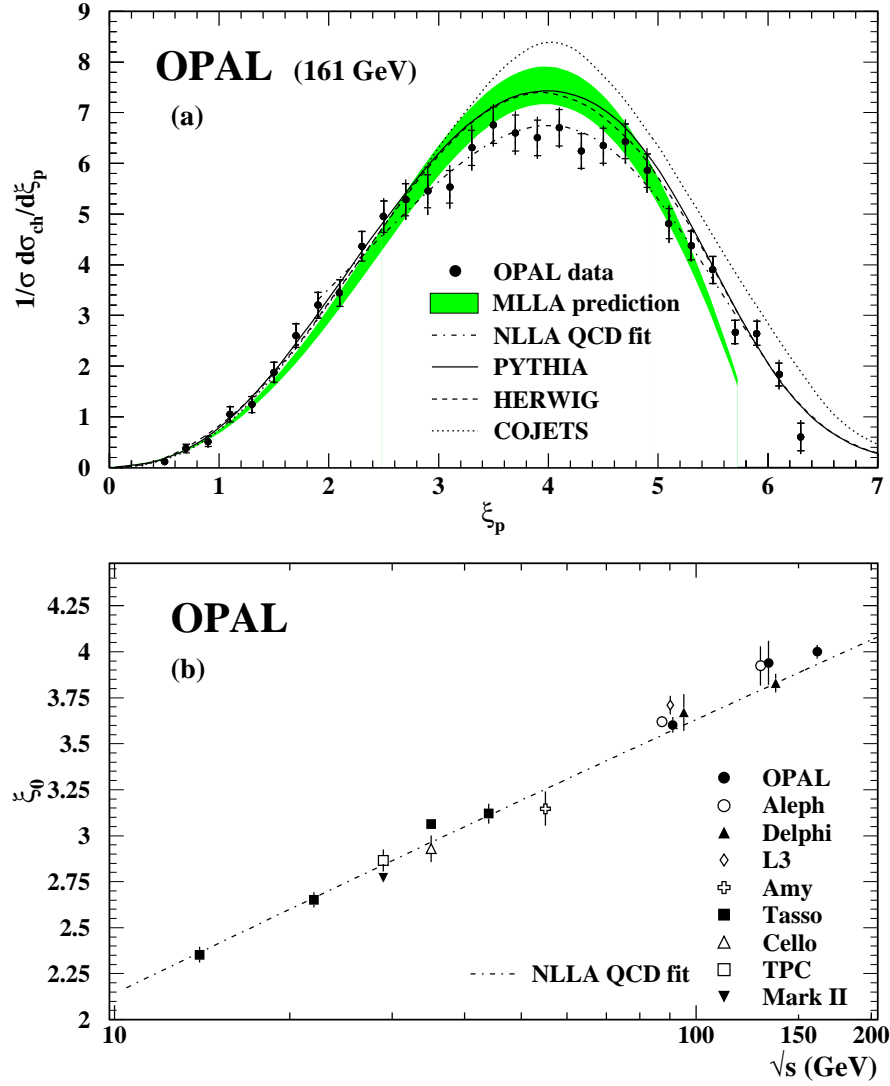
Fig. 5. (a) Distribution of $\xi_p = \ln(1/x_p)$ for charged particles. Also shown are the MLLA QCD prediction and the predictions of several Monte Carlo generators. (b) Evolution of the position of the peak of the ξ_p distribution, ξ_0, as a function of $\sqrt{s}$, compared with a fit of a NLLA QCD prediction up to and including the data points at $\sqrt{s} = 130$ GeV.
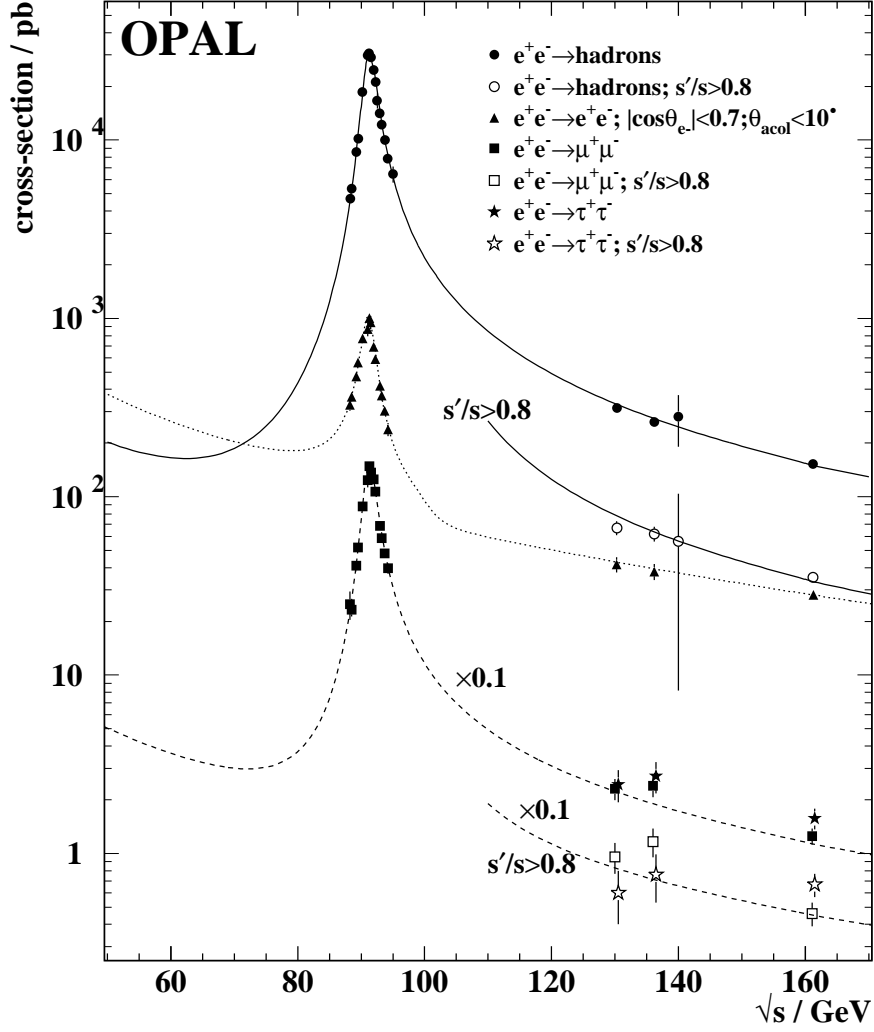
Fig. 6. Measured total cross-sections ($s'/s > 0.01$) for different final states as a function of $\sqrt{s}$. The cross-sections for $\mu^+\mu^-$ and $\tau^+\tau^-$ production have been reduced by a factor of ten for clarity. For the $q\bar{q}$, $\mu^+\mu^-$, and $\tau^+\tau^-$ final states, the cross-sections at high energies ($\sqrt{s} \geq 130$ GeV) are also shown for $s'/s > 0.80$. The curves show the SM predictions of ZFITTER and ALIBABA.
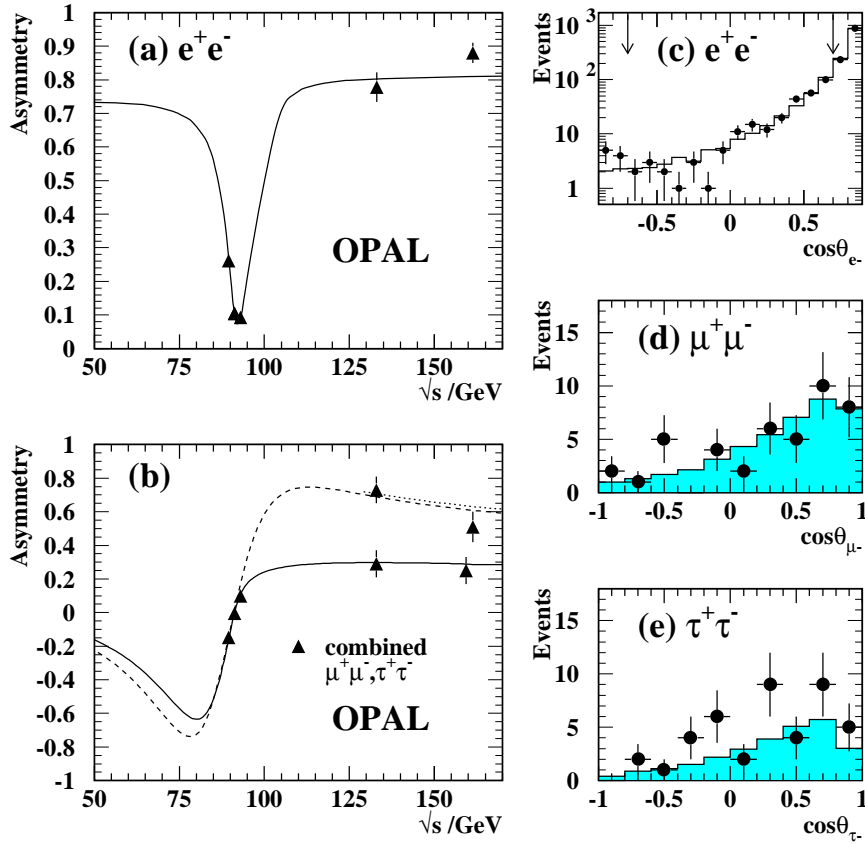
Fig. 7. (a) Measured forward-backward asymmetry for e^+e^- pairs selected with $|\cos\theta_{e^-}| < 0.7$ and $\theta_{\mathrm{acol}} < 10°$ as a function of $\sqrt{s}$. The curve shows the prediction of ALIBABA. (b) Measured asymmetries for the inclusive and exclusive samples of $\mu^+\mu^-$ and $\tau^+\tau^-$ combined. The curves show the predictions from ZFITTER for the inclusive (solid) and exclusive (dotted) selections as well as the Born-level expectation without QED radiative effects (dashed). The observed $\cos\theta$ distributions of the outgoing lepton are shown in (c) to (e) (points) and are compared with Monte Carlo expectations (histograms). The arrows in (c) show the position of the cuts at $|\cos\theta_{e^-}| < 0.7$.
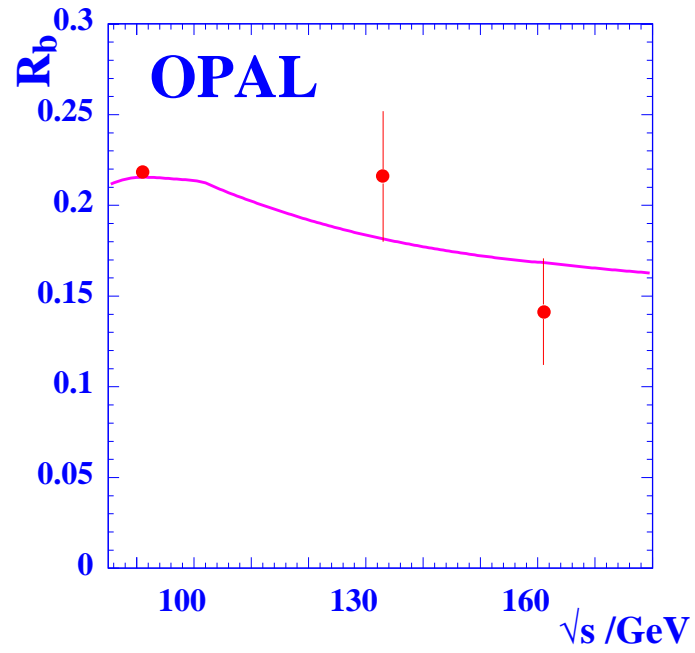
Fig. 8. R_b as a function of $\sqrt{s}$. The points are the OPAL measurements and the solid line is the ZFITTER prediction. The errors are the quadrature sum of the statistical and systematic contributions.
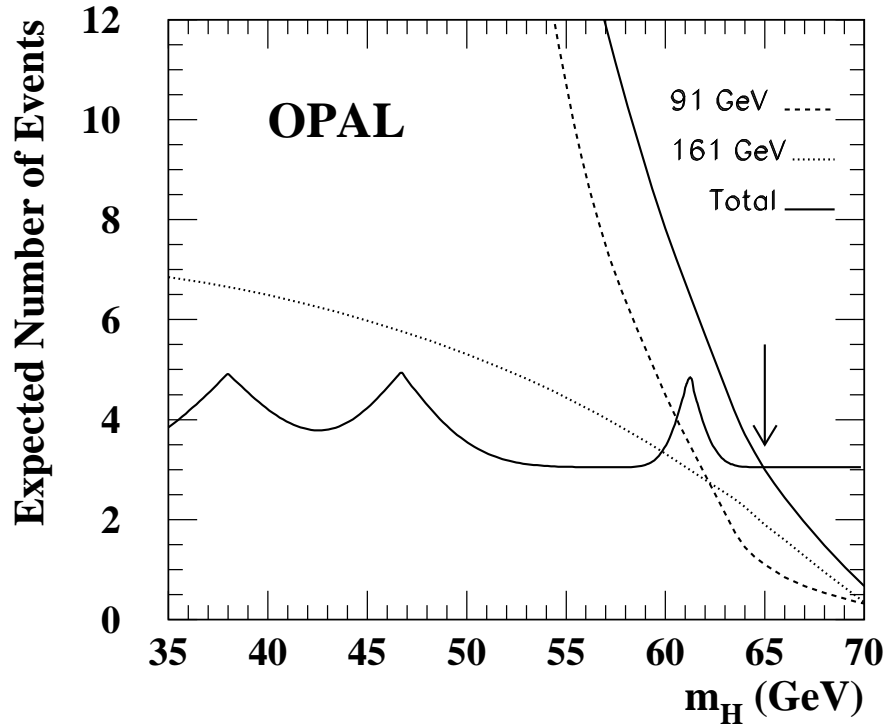
Fig. 9. Expected number of events as a function of the Higgs boson mass, M_H, for the search at $\sqrt{s} = 161.3$ GeV (dotted), and at $\sqrt{s} \approx M_Z^0$ (dashed). Combining the searches yields the expectation given by the falling solid line. The 95% confidence level upper limit in the presence of three candidate events is given as the solid horizontal curve. The intersection of the two solid curves, indicated by the arrow, determines our 95% confidence level lower limit on the Higgs boson mass.
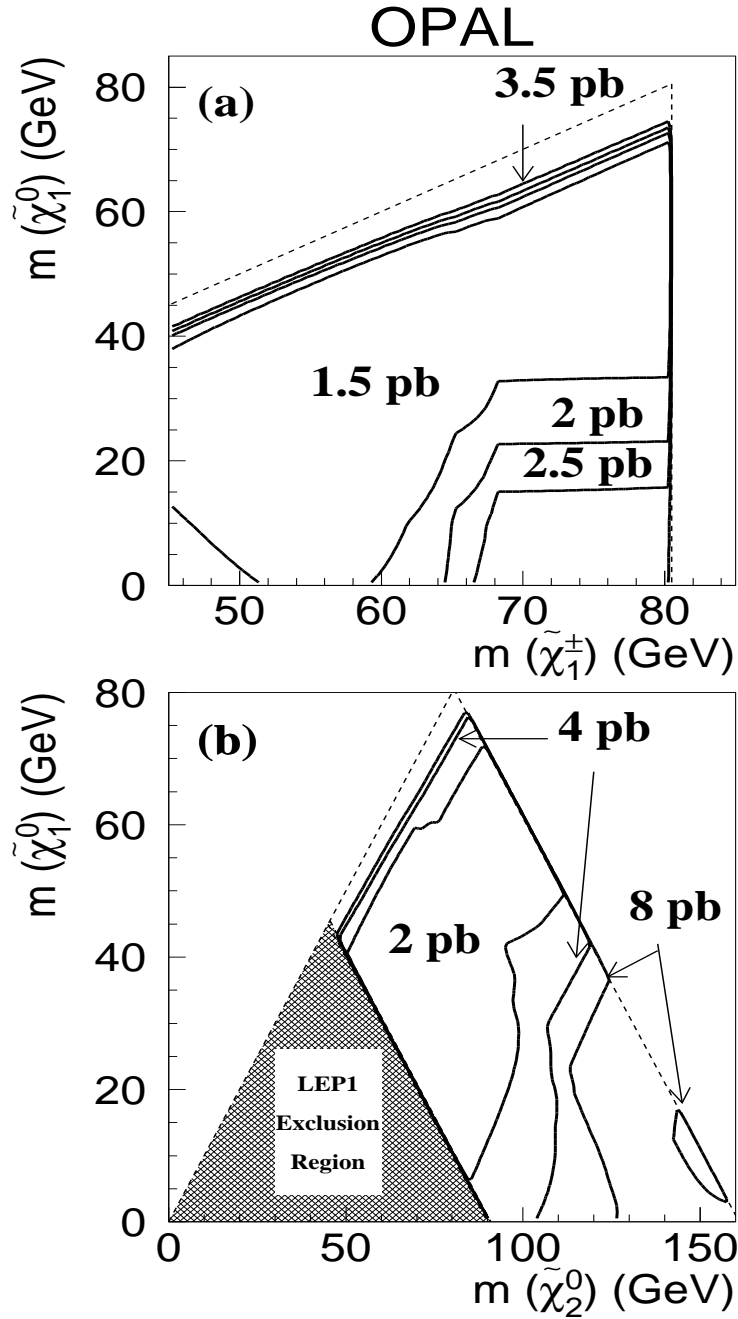
Fig. 10. The 95% confidence level production cross-section contours for (a) $e^+e^- \rightarrow \tilde{\chi}_1^+\tilde{\chi}_1^-$, and (b) $e^+e^- \rightarrow \tilde{\chi}_1^0\tilde{\chi}_2^0$ assuming the decays $\tilde{\chi}_1^\pm \rightarrow \tilde{\chi}_1^0 W^{*\pm}$ and $\tilde{\chi}_2^0 \rightarrow \tilde{\chi}_1^0 Z^*$ occur with 100% branching fraction. These limits have been obtained by combining the results of the $\sqrt{s} = 161$ GeV and $\sqrt{s} = 130 - 136$ GeV analyses [23].
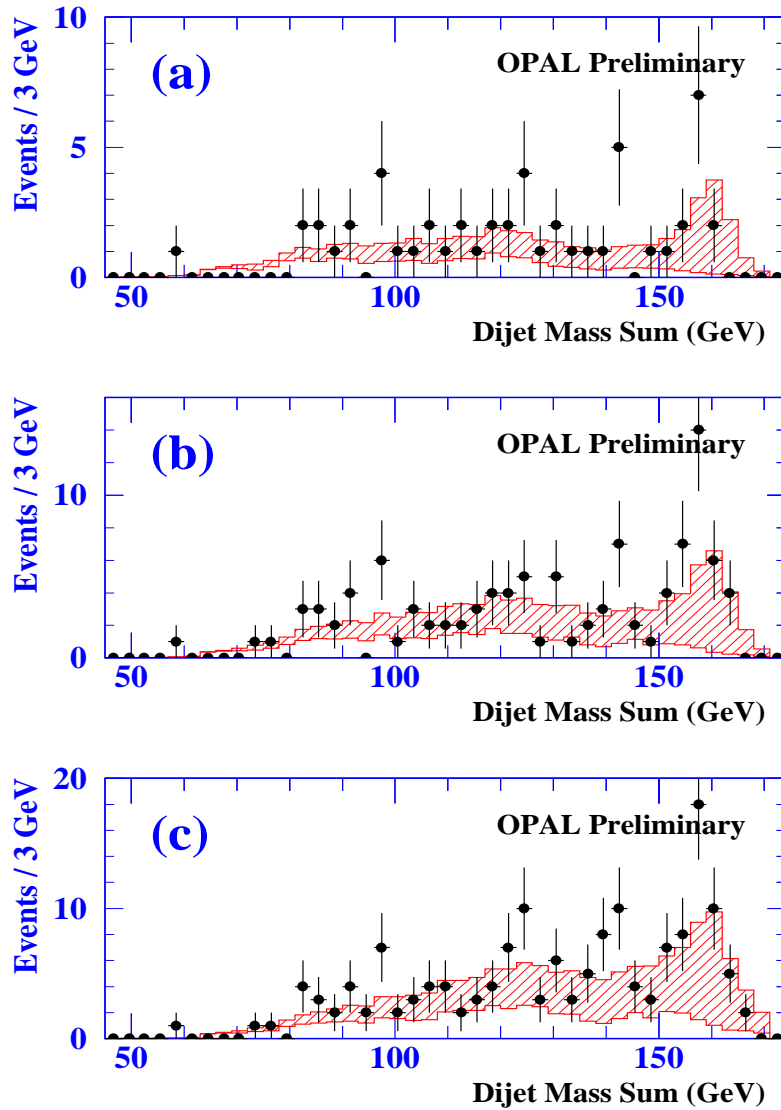
Fig. 11. Distribution of the dijet mass sum in 4-jet events for OPAL data combined from all data samples ($\sqrt{s} \geq 130$ GeV) after all cuts in the search for anomalous 4-jet production. No W-pair veto has been applied. Plot (a) shows the distribution for the combination with the minimum dijet mass difference, ΔM, plot (b) accumulates the contributions from combinations for the smallest and the intermediate ΔM, and plot (c) contains contributions from all three combinations. Data are shown by points and SM backgrounds by the histogram. The hatched component of the background histogram denotes four-fermion processes (predominantly W$^+$W$^-$), while the unhatched component denotes Z$^0/\gamma \to q\bar{q}$.
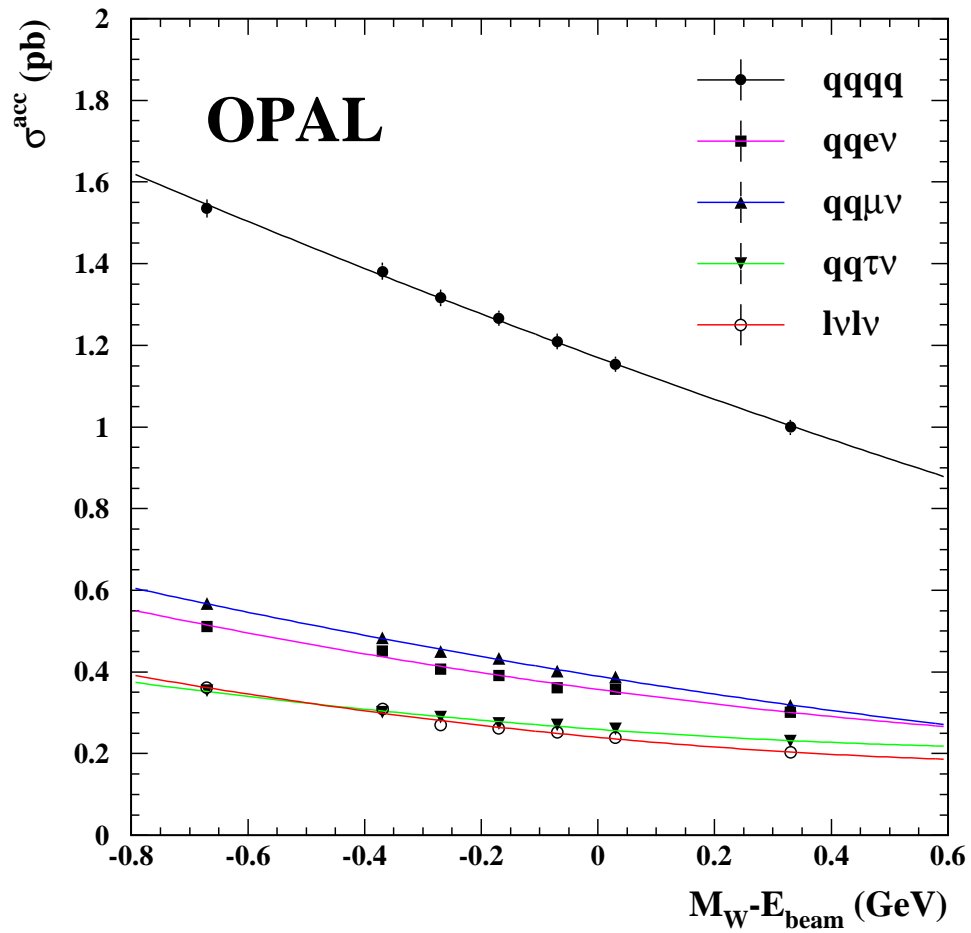
Fig. 12. The accepted cross-sections for each W^+W^- decay channel as a function of $M_W - E_{beam}$. In each case the functional dependence is parametrised by a second order polynomial. These are used in extracting the mass of the W boson and implicitly account for the four-fermion interference effects.
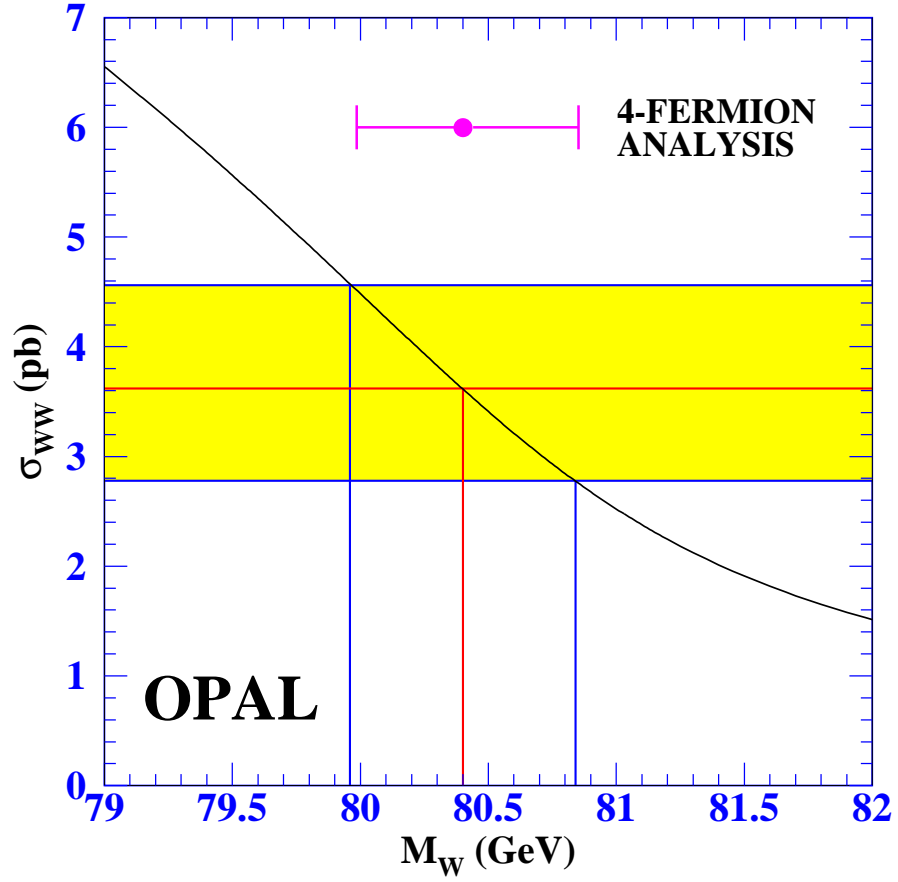
Fig. 13. Distributions of σ_{WW} as a function of M_W as predicted by the semi-analytic program GENTLE for $\sqrt{s} = 161.3$ GeV. The measured W^+W^- cross-section is shown as a shaded band and the corresponding W boson mass by vertical lines. For comparison, our principal measurement of M_W is shown as a point with error bars. The uncertainties include statistical and systematic contributions, but do not include the effect of the beam energy uncertainty.
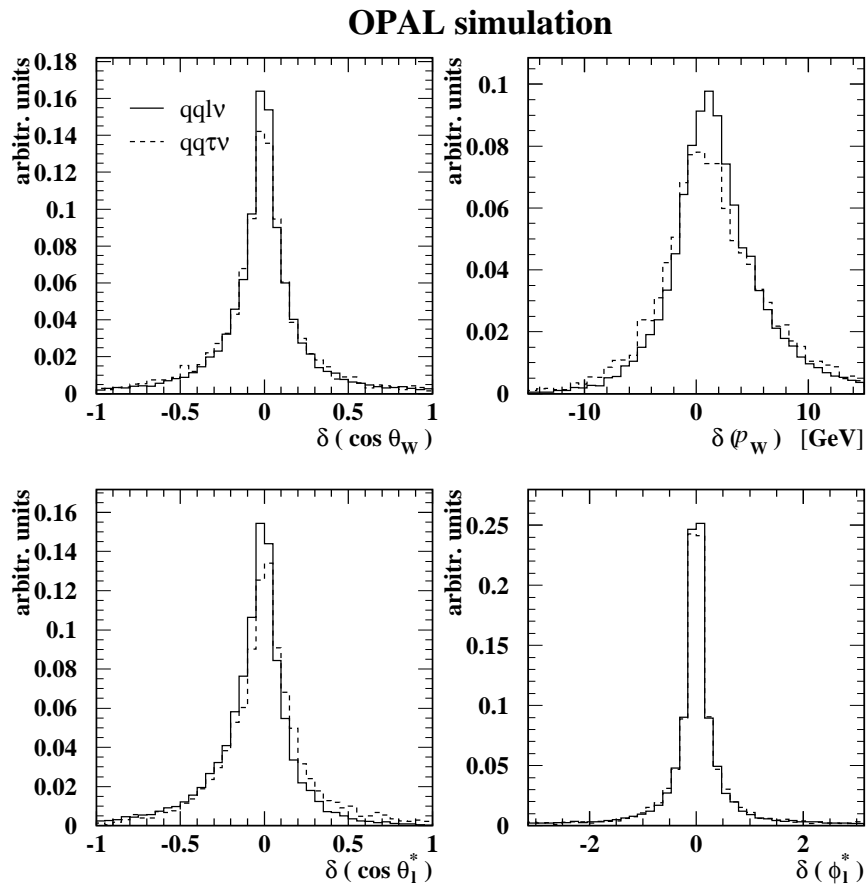
Fig. 14. The resolution of the kinematic variables from the $q\bar{q}\ell\nu$ events used in the TGC analysis. All distributions show the difference between reconstructed and generated quantities. The solid line is for $q\bar{q}e\nu$ and $q\bar{q}\mu\nu$ events and the dashed line is for $q\bar{q}\tau\nu$ events.
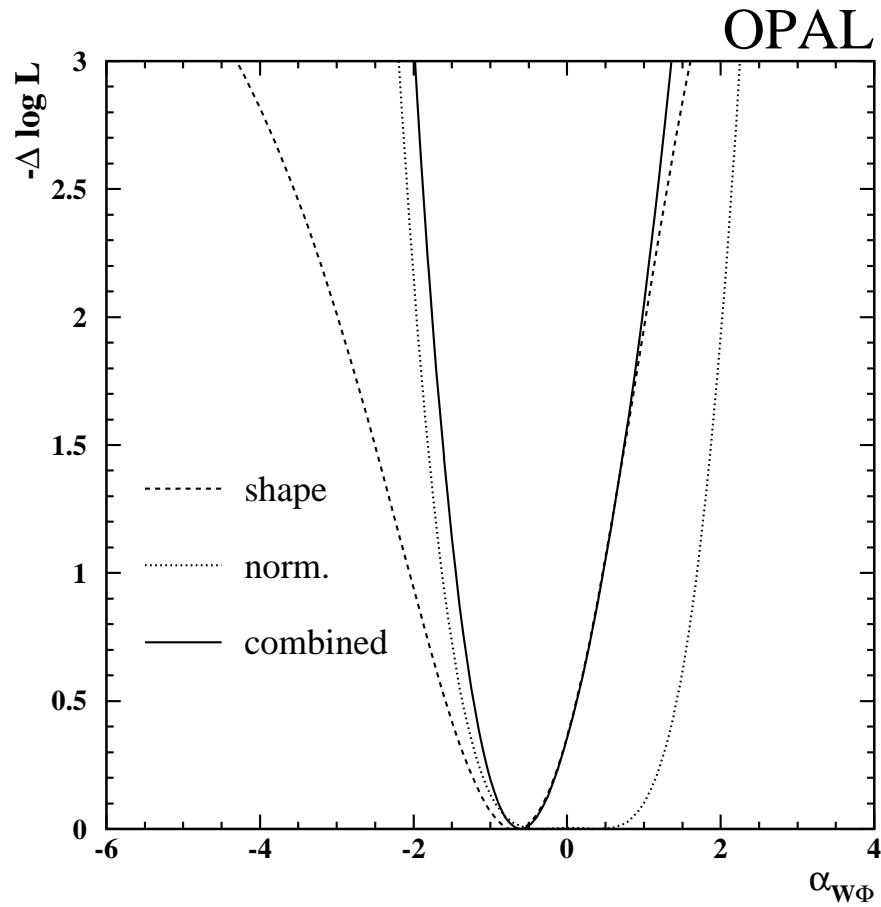
Fig. 15. Likelihood distributions obtained from the cross-section (dotted) and differential distributions (dashed) for the TGC analysis. The solid line is the distribution obtained by adding these together. In all cases the minimum value of the negative log likelihood has been subtracted.